Fermilab FERMILAB-FN-0728 January 2003

Pathlength Fluctuations in Thick Targets

A. Van Ginneken
Fermi National Accelerator Laboratory*
P. O. Box 500, Batavia, IL 60510

December 2002

Abstract

Fluctuations in pathlength of muons traversing matter are studied by means of the Gaussian approximation in the context of Monte Carlo simulations of muon transport. The method estimates the muon's pathlength corresponding to a Monte Carlo step from a knowledge of the transverse phase space variables at the beginning and end of the step. The step is then halved and pathlength is recalculated. This is repeated until the result is stable to within a desired tolerance. An extension to the case where electromagnetic fields are present is described. A few results obtained with this method are presented by way of illustration.

1 Introduction

Muon ionization cooling is more effective at relatively low energies. Current scenarios favor kinetic energies of 100–300 MeV but some muons may well stray outside this range while traversing a typical cooling channel. Especially, at the lower end of this extended range straightforward use of the small angle and related approximations—which permeates much of the analyses and simulation codes—may be questioned. In particular, pathlengths through matter may not always be accurately evaluated. In simulations, an accurate measure of the pathlength is needed to calculate averages of energy loss and angular deflection as well as fluctuations about the averages. Pathlength fluctuations also affect time of arrival at an RF cavity and thus the accelerating voltage applied to the muon. Good estimates of pathlength

*Work supported by the U.S. Department of Energy under contract No. DE-AC02-76CHO3000.

are therefore essential to the analysis of any proposed cooling channel. This Note presents a method to estimate pathlength distributions of muons after traversing a thick target—in which an electromagnetic field may be present. The method may eventually evolve into a workable algorithm—for use in more comprehensive codes of particle transport—but this is not the goal here.

In this Note, the small angle approximation is used as part of a perturbative/iterative approach to pathlength estimation. In Monte Carlo calculations it is convenient to simulate collisions of muons with nuclei or electrons *collectively*—using the small angle approximation—below some assumed threshold angle, while above it collisions are simulated *individually* with full 3-D treatment [1]. In principle, increasing the fraction of events treated individually leads to an (almost) full 3-D event-by-event simulation of the problem. In practice, due to decreasing step size, the energy– and angular distribution of the events treated collectively become increasingly skewed and harder to sample by any *a priori* adopted algorithm.

Sec. 2 reviews the relevant probability distribution and presents the basic strategy used in estimating pathlength. This involves first transporting the muon across a fixed step in the beam's general direction, z, then making adjustments to the muon's phase space variables as an improved approximation to the trajectory is determined. The procedure for assigning values to the phase space variables after the initial step is outlined in Sec. 3. Sec. 4 describes the use of 'random interpolation' to make improved pathlength estimates and—in turn—improved estimates of the phase space variables at the end of the step. Adaptation of the algorithms to the presence of electromagnetic fields is discussed in Sec. 5. Some results obtained with the new algorithms are shown in Sec. 6. A few concluding remarks are in Sec. 7.

2 Basic Algorithm

The procedure adopted here takes steps of fixed length along z. Only 'slab' geometries are dealt with. Values of the resulting (projected) angular deflections, x', y', and energy loss, ε, are estimated by the algorithms of [1]. This includes sampling from realistic collective distributions as well as simulating discrete processes on an event-by-event basis. The pathlength assumed in this step is an average pathlength as derived from the basic arc length formula. Subsequently, two basic correction procedures are introduced to improve pathlength estimates and its impact on phase space variables: *end point adjustment* and midpoint *random interpolation*. End point adjust-

ment involves estimating the change in pathlength to reflect the *a posteriori* knowledge of the phase space variables at the end of the step—which in turn induces a small correction on these same phase space variables. Random interpolation refers to choosing an interpolating value, at some point intermediate in z, from a probability distribution which incorporates the known end point values as parameters. This also influences pathlength and induces another correction to the phase space variables. *In vacuo*, with an electromagnetic field present for which orbits are not easily calculated by analytical means, a common strategy is to divide the initial step into two or more pieces and compare results with those of the full step. If necessary, this can be repeated until results of successive step-divisions meet some specified criterion. As such, this strategy won't work in transport *through matter* because of the inherent randomness involved in scattering and energy loss. In the present study successive step division is retained but—at each midpoint—*random* values are chosen for the phase space values in a manner consistent with what is already known about the trajectory. In contrast with the full (initial) step treatment, these random interpolations are based on the Gaussian approximation.

2.1 Gaussians

To evaluate pathlength corrections the method adopted here makes use of the bi-Gaussian Fermi distribution [2, 3] for multiple scattering:

$$\begin{aligned} F(x,x'|x_0,x_0',z) &= (2\sqrt{3}/\pi\theta_s^2 z^2) \\ &\times\ e^{-(4/\theta_s^2 z)\left[(x'-x_0')^2-3(x'-x_0')(x/z-x_0/z-x_0')+3(x/z-x_0/z-x_0')^2\right]} \end{aligned} \tag{1}$$

where x_0, x, x_0', x' are, resp., the initial and final x-coordinates and their derivatives with respect to z, while θ_s^2 is the mean square (polar) scattering angle per unit length. As per custom, the symbol $|$ in Eq. 1 separates the unknowns x, x' from the given variables x_0, x_0', z. There is an entirely similar distribution for y, y', independent of x, x'. This should be borne in mind throughout this Note.

At some (low) level of approximation, energy loss in a thick target is also represented by a Gaussian [2], $G(\varepsilon|\overline{\varepsilon},\sigma_\varepsilon)$, where ε is the energy observed at depth z in the target and

$$\overline{\varepsilon} = \varepsilon_0 - \left|\frac{dE}{dx}\right| \ell \tag{2}$$

is the average energy expected there, while

$$\sigma_\varepsilon^2 = 2\pi N_{Av} Z e^4 T_{max}(1-\beta^2/2)\overline{\ell}/A\beta^2 \tag{3}$$

with T_{max} the maximum energy transferable by the muon to a stationary free electron, $\overline{\ell}$ is the estimated average pathlength at depth z (see Sec. 3.1 below), and the other symbols have their ususal meaning.

2.2 Large Angles, Energy Loss

As is well known, the Gaussian distribution of x', i.e., the marginal distribution in x' of Eq. 1, severely underestimates what is observed at large x' or predicted there by a more accurate description such as the Molière distribution. One remedy, favored here, is to introduce a cut-off angle in the $\mu N(\mu e)$ scattering cross section. Below this cut-off events are treated collectively by means of a *modified* Gaussian—in the form of an Edgeworth series [1]—while above it events are simulated individually. This is simpler than sampling from the Molière distribution and at the same time more accurate: even complicated nuclear form factors are readily included in the large-angle part while individual event simulations automatically include correlations between angular deflection and energy loss. Incoherent nuclear scattering with ejection of a nucleon may also be included among the individual processes.

For essentially the same reasons, a cut-off is used in the algorithms which estimate energy loss. Above it muon-electron scattering events are simulated individually while below it events are combined into a 'restricted' Vavilov-type distribution [4] which may also be conveniently approximated by an Edgeworth series [1].

In both the angle and energy loss determinations an additional source of pathlength fluctuation results from the variable number of individual encounters. For the large number of small angle, small energy loss encounters—summed over a target of reasonable thickness—such fluctuations are typically negligible. However, these fluctuations may matter when sampling events above the cut-off angle or energy. Thus the number of events simulated individually is chosen from a Poisson distribution determined by the average number of such events. Thresholds for individual treatments must therefore be set low enough so that fluctuations of this type are adequately explored.

2.3 Corrections

Only after initial selection is complete does the procedure make use of Eqs. 1 and 3 to evaluate corrections to x, y, x', y', and energy loss. Because these corrections are applied to all angles and energy losses encountered—

including those simulated by discrete processes—the parameters θ_s and σ_ε of these distributions must be evaluated over the *whole* range of allowed values whereas similar parameters in the (collective) algorithms of [1] are *restricted* by cut-off energies or angles.

Muons are followed through a specified geometry in steps of fixed length in the z-direction. This could be adapted to steps measured along a curved central trajectory. Such a step is then split sequentially into 2,4,8,... steps and, after each such split, x, x', y, y', t, ℓ at the end of the entire step are obtained. To aid in the convergence, Richardson extrapolation [5] is performed on each variable. Thus a variable, such as x at the end of a z-step, having been determined for a sequence of decreasing steplengths, is now considered as a function of steplength which is then extrapolated to zero. Comparison for stability with respect to user specified toleranace is performed on the extrapolated results for pathlength. Pathlength is chosen since it is the object of the present study and since it appears more sensitive to steplength than the usual phase space variables

3 Initial Step

Tracking a muon begins by taking a fixed z-step through the geometry. The choice of initial steplength must reflect material density and—where relevant—field strengths. Steplength can be adjusted as the calculation proceeds to reflect a changing environment or take into account information gained from previous steps. Correlations between energy loss and angular distribution are included in angle and energy selection algorithms for the initial step. In the adjustment stage the relatively small changes to angular deflection and energy loss, based on Eqs. 1 and 3, are made independently but all correlations present in the initial full step are preserved.

3.1 Initial Pathlength Estimate

Prior to entering a z-slice, let the muon coordinates be x_0, y_0 and its direction x'_0, y'_0. Without any scattering the pathlength in a z-step is $\ell_0 = z/\cos\theta_0 = zp_0/p_z$, where θ_0 is the spatial angle of the incident muon with respect to the z-axis. From this estimate, average energy loss and *rms* scattering angle are determined using as input energy and momentum at (projected) mid-step. The pathlength, ℓ_1, through the z-slice of thickness z_1 is estimated from the usual parametric formula for arc length using z as the parameter:

$$\ell_1 = \int_0^{z_1} \frac{dz}{\cos\theta} = \int_0^{z_1} \left(1 + x'^2 + y'^2\right)^{1/2} dz$$

$$\approx \int_0^{z_1} \left[1 + \frac{1}{2}\left(x'^2 + y'^2\right) - \frac{1}{8}\left(x'^2 + y'^2\right)^2\right] dz. \tag{4}$$

In Eqs. 4, x' and y' at coordinate z are *random* variables. If it is assumed that they follow a Gaussian distribution, the averaged pathlength becomes:

$$\begin{aligned} \overline{\ell_1} &\approx \int_0^{z_1}\int_{-\infty}^{\infty}\int_{-\infty}^{\infty}\left[1 + \frac{1}{2}\left(x'^2 + y'^2\right) - \frac{1}{8}\left(x'^2 + y'^2\right)^2\right] \\ &\times G(x'|\overline{x'}, \sigma_{x'})G(y'|\overline{y'}, \sigma_{y'})dx'dy'dz \\ &= \int_0^{z_1}\left[1 + \frac{1}{2}\left(\overline{x'^2} + \overline{y'^2}\right) - \frac{1}{8}\left(\overline{x'^4} + 2\overline{x'^2y'^2} + \overline{y'^4}\right)\right] dz. \end{aligned} \tag{5}$$

For a Gaussian distribution in general, $\overline{x'^2}$ and $\overline{x'^4}$ are readily obtained:

$$\begin{aligned} \overline{x'^2} &= \overline{x'}^2 + \sigma_{x'}^2 \\ \overline{x'^4} &= \overline{x'}^4 + 6\overline{x'}^2\sigma_{x'}^2 + 3\sigma_{x'}^4. \end{aligned} \tag{6}$$

The Gaussian distribution of relevance here is the marginal distribution in x' of Eq. 1. Its parameters are $\overline{x'} = x'_0$ and $\sigma_{x'} = \theta_s(\ell/2)^{1/2}$ with $\ell = p_0 z/p_z$. Substituting into Eqs. 6:

$$\begin{aligned} \overline{x'^2} &= x_0'^2 + \frac{1}{2}\theta_s^2\left(p_0/p_z\right)z \\ \overline{x'^4} &= x_0'^4 + 3x_0'^2\theta_s^2\left(p_0/p_z\right)z + \frac{3}{4}\theta_s^4\left(p_0/p_z\right)^2 z^2 \end{aligned} \tag{7}$$

and then integration of Eq. 5 over z yields:

$$\begin{aligned} \overline{\ell_1} &= \left[1 + \frac{1}{2}(x_0'^2 + y_0'^2) - \frac{1}{8}(x_0'^2 + y_0'^2)^2\right] z_1 \\ &+ \frac{1}{4}\left[1 - (x_0'^2 + y_0'^2)\right]\theta_s^2(p_0/p_z)z_1^2 - \frac{1}{12}\theta_s^4(p_0/p_z)^2 z_1^3. \end{aligned} \tag{8}$$

The part inside the first square brackets of Eq. 8 can be identified with the first three terms of the expansion of $\sqrt{1 + x_0'^2 + y_0'^2} = p_0/p_z$. Making this substitution should provide a good estimate for the average pathlength at this level of approximation and at this juncture in the simulation:

$$\overline{\ell_1} = z_1\frac{p_0}{p_z}\left[1 + \frac{1}{2}\theta_s^2 z_1 - \frac{1}{4}\left(\frac{p_0}{p_z}\right)^2\theta_s^2 z_1 - \frac{1}{12}\left(\frac{p_0}{p_z}\right)\theta_s^4 z_1^2\right]. \tag{9}$$

This $\overline{\ell_1}$ is now used to determine the average energy loss and *rms* scattering angle upon which random selection of x'_1, y'_1 and energy loss—via the algorithms of [1]—is based. Then, given x'_1, the coordinate x_1 at z_1 is selected

from the *conditional* distribution of x at z_1. This is also a Gaussian as follows from substituting x_1' for x' in Eq. 1: $G(x|x_0 + (x_0' + x_1')z_1/2, \theta_s \overline{\ell_1}^{3/2}/2\sqrt{6})$. In calculating corrections to these initial estimates it is clear that z, as it occurs, e.g., in Eq. 1, should be replaced by ℓ also.

3.2 Pathlength Adjustment

Next, the (average) pathlength is adjusted to reflect the choices made for x, y, x', y' at the end of the z-slice—which, in turn, leads to readjustment of these same variables. The distribution of x' at any depth z, given the values of x_0, x_0', x_1, x_1' at beginning and end, is again Gaussian and is obtained by integrating $F\left(x, x'|x_0, x_0', x_1, x_1', z\right)$ over all x, where

$$F\left(x, x'|x_0, x_0', x_1, x_1', z\right) = \frac{F\left(x, x'|x_0, x_0', z\right) F\left(x_1, x_1'|x, x', z_1 - z\right)}{F\left(x_1, x_1'|x_0, x_0', z_1\right)} \tag{10}$$

as follows from Bayes' Theorem and where the F's in the RHS are all as per Eq. 1. Carrying out this integration yields the Gaussian parameters:

$$\begin{aligned}
\overline{x'}(z) &= x_0' + \frac{z}{z_1}\left(x_1' - x_0'\right) + \frac{3z(z_1 - z)}{z_1^2}\left(2\frac{x_1 - x_0}{z_1} - \left(x_1' + x_0'\right)\right) \\
\sigma_{x'}^2(z) &= \frac{\theta_s^2 \overline{\ell} z\left(z_1 - z\right)\left[z^3 + \left(z_1 - z\right)^3\right]}{2z_1^5}.
\end{aligned} \tag{11}$$

Integration of Eq. 5, with substitution from Eqs. 11, results in a rather cumbersome expression:

$$\overline{\ell}_{nw} = z_1\left(1 + \frac{1}{2}I_x + \frac{1}{2}I_y + I_\sigma - \frac{1}{8}I_{xy} - I_{x\sigma} - I_{y\sigma} - I_{\sigma\sigma}\right) \tag{12}$$

where

$$\begin{aligned}
I_x &= S_x^2 + \frac{1}{5}\left(S_x - M_x\right)^2 + \frac{1}{12}V_x^2 \\
I_\sigma &= \frac{\theta_s^2 \overline{\ell_1}}{30} \\
I_{xy} &= \frac{72}{35}\left(S_x^2 + S_y^2\right)^2 + \frac{3}{35}\left(M_x^2 + M_y^2\right)^2 + \frac{1}{80}\left(V_x^2 + V_y^2\right)^2 \\
&+ \frac{9}{35}\left(S_xV_x + S_yV_y\right)^2 + \frac{36}{35}\left(M_xS_x + M_yS_y\right)^2 + \frac{11}{70}\left(M_xV_x + M_yV_y\right)^2 \\
&+ \frac{3}{35}\left(S_xV_y - S_yV_x\right)^2 + \frac{12}{35}\left(M_xS_y - M_yS_x\right)^2 + \frac{11}{210}\left(M_xV_y - M_yV_x\right)^2 \\
&- \frac{1}{35}\left(M_xS_x + M_yS_y\right)\left[72\left(S_x^2 + S_y^2\right) + 4\left(M_x^2 + M_y^2\right) - \left(V_x^2 + V_y^2\right)\right]
\end{aligned}$$

$$
\begin{aligned}
&+ \quad \frac{2}{35}\left(M_x V_x + M_y V_y\right)\left(S_x V_x + S_y V_y\right) \\
I_{x\sigma} &= \frac{\theta_s^2 \overline{\ell_1}}{420}\left(2M_x^2 - 6M_x S_x + 18 S_x^2 + V_x^2\right) \\
I_{\sigma\sigma} &= \frac{\left(\theta_s^2 \overline{\ell_1}\right)^2}{840}
\end{aligned} \tag{13}
$$

with abbreviations $S_x = (x_1 - x_0)/z_1, M_x = (x_1' + x_0')/2, V_x = x_1' - x_0'$, and with similar definitons for I_y and $I_{y\sigma}$.

Adjustments are now made to the phase space variables at the end of the step to reflect the improved pathlength estimate, $\overline{\ell_{nw}}$, by simple rescaling. While Gaussians are used only in the adjustment stage, it may be assumed *pro forma* that the more laboriously generated phase space variables of the initial step are the result of Gaussian random selection: e.g., $x' = \overline{x'} + r_G \sigma_{x'}$, where r_G represents a Gaussian random variate with zero mean and unit variance. Since $\sigma_{x'}$ scales with $\ell^{1/2}$ this leads to

$$
x'_{nw} = \overline{x'} + \left(x_1' - \overline{x'}\right)\left(\frac{\overline{\ell_{nw}}}{\overline{\ell_1}}\right)^{1/2}. \tag{14}
$$

Likewise, x is rescaled:

$$
x_{nw} = \overline{x} + (x_1 - \overline{x})\left(\frac{\overline{\ell_{nw}}}{\overline{\ell_1}}\right)^{3/2} \tag{15}
$$

where $\overline{x} = x_0 + (x_0' + x_1')\, z_1/2$ as per Sec. 3.1. Similarly, energy loss and elapsed time may be corrected using the new pathlength but to save computation this is postponed until convergence is achieved for average pathlength. Considering the effects of a small adjustment in energy on *rms* scattering angle this appears justified. It may not apply when EM-fields are present, see below.

At this point a first iteration is initiated: x_{nw}, x'_{nw} replace x_1, x_1' in Eqs. 11 and, along with y_{nw}, y'_{nw}, determine a new $\overline{\ell_{nw}}$ which leads to a new x_{nw}, x'_{nw}, etc., until convergence (in $x, x', y, y', \overline{\ell_{nw}}$) is achieved to some specified tolerance.

4 Random Interpolation

Random interpolation consists of selecting x, x', y, y' at an intermediate location, *here always chosen mid-step along* z, in a manner consistent with the known values of these variables at the neighboring end points. Independence

of events for scattering and energy loss means that only nearest-neighbors need be considered. Adopting specific values for intermediate x, x', y, y' in this manner thus leads to a path winding through initial, final, and all intermediate locations with crossing angles as determined at each stage by random interpolation. At the set of 'in-between' z-segments the trajectory remains free but the probability distributions of x, x', y, y' at these locations center more narrowly about their average values with successive subdivisions. Random interpolation may also be performed for the energy (and time) variable if variation in energy over a steplength affects θ_s significantly. As a practical matter this should seldom be necessary. As in the case of end point adjustments, above, energy and time calculation is postponed until convergence is achieved.

In the present study—until the final stage is reached—it is *average* pathlength which is adopted to adjust angles and positions as well as to check on convergence of the calculation. It might seem appropriate to choose—at each stage, beginning with the initial step—a *random* pathlength using an appropriate distribution based on what is known about the path at that point. However, complications arise if further subdivision proves necessary, i.e., if one must determine new intermediate x, x', y, y' which would then depend (in some complicated manner) upon the pathlength chosen randomly in the previous iteration(s). This is avoided by using the average pathlength at all stages of the iteration until the final one when this difficulty is not present and a random value is chosen from a Gaussian (see Sec. 4.3).

4.1 Angles, Positions

At some intermediate location—and with x as yet unspecified—x' is distributed as a Gaussian, already encountered above, with parameters given by Eqs. 11. Once a value of x' is chosen at some intermediate point, z, the distribution of x at that point is also Gaussian with:

$$\begin{aligned}
\overline{x}(z) &= \frac{(z_1 - z)^3 \left[(x' + x'_0)\, z + 2x_0\right] - z^3 \left[(x' + x'_1)\,(z_1 - z) - 2x_1\right]}{2\left[z^3 + (z_1 - z)^3\right]} \\
\sigma_x^2(z) &= \frac{\theta_s^2 \overline{\ell_{nw}}^3 z^3 (z_1 - z)^3}{24 z_1^3 \left[z^3 + (z_1 - z)^3\right]}. \qquad (16)
\end{aligned}$$

Since—in this study—the interpolation point is always midway (in z) between the endpoints Eqs. 11 simplify considerably:

$$\overline{x'} = \frac{3\,(x_1 - x_0)}{2z_1} - \frac{1}{4}\,(x'_0 + x'_1)$$

$$\sigma_{x'}^2 = \frac{\theta_s^2 \overline{\ell_{nw}}}{32} \tag{17}$$

as do Eqs. 16:

$$\begin{aligned} \overline{x} &= \frac{(x_1 + x_0)}{2} - \frac{1}{8}\left(x_1' - x_0'\right) z_1 \\ \sigma_x^2 &= \frac{\theta_s^2 \overline{\ell_{nw}}^3}{384}. \end{aligned} \tag{18}$$

As can be seen—at the midway point, but not elsewhere—the x-distribution is independent of the x'-value selected. Having chosen intermediate x, x', y, y' as per Eqs. 17 and 18 the new pathlength can now be estimated using Eq. 12 as the sum of the two legs. Knowing the new pathlength, adjustments are made to the x_1, x_1', y_1, y_1' at the end of the step as per Eqs. 14 and 15.

4.2 Convergence

Following determination of all variables at the end of a z-slice, Richardson extrapolation is performed and the predicted average pathlength is compared with that obtained in the previous round. If they do not match within specified tolerance a new subdivision is initiated. As the number of subdivisions of the z-slice is increased, the order of the polynomial (in h, the width of the subdivision) of the Richardson extrapolation increases. The order of the polynomial keeps pace with the subdivisions until the fourth order after which it is kept at that level and only the values corresponding to the four smallest subdivisions participate in the extrapolation. Only even orders of h are considered since this guarantees the residuals of the phase space variables to have a minimum at $h = 0$ [5].

4.3 Final Adjustments

At the end of this process—when successive iterations agree on the average value of the pathlength to within tolerance—a final adjustment is made to allow a random variation of the pathlength given the parameters which have been fixed thus far. This variation reflects what may occur along all the in-between z-segments where the phase space variables are not fixed. At each stage of the subdivision, the average value of the pathlength of the ith segment, $\overline{\ell_i}$, is known. It is assumed that the pathlength distribution is Gaussian about this average. Its variance is estimated from the usual propagation-of-errors formula

$$\sigma_\ell^2 = \left(\frac{\partial \ell}{\partial x'}\right)^2 \sigma_{x'}^2 + \left(\frac{\partial \ell}{\partial y'}\right)^2 \sigma_{y'}^2. \tag{19}$$

The partial derivatives—for the ith subdivision—follow from Eq. 4, evaluated to lowest order

$$\frac{\partial \ell}{\partial x'} \approx \int_{z_i}^{z_{i+1}} x' dz = x_{i+1} - x_i \tag{20}$$

while $\sigma_{x'}^2$ is represented by its average over the trajectory

$$\overline{\sigma_{x'}^2} = \frac{\int_{z_i}^{z_{i+1}} \sigma_{x'}^2(z) dz}{z_{i+1} - z_i} \tag{21}$$

where $\sigma_{x'}^2(z)$ is taken from Eqs. 11. Performing the integration and adding the y-term yields:

$$\sigma_{\ell_i}^2 = \left[(x_{i+1} - x_i)^2 + (y_{i+1} - y_i)^2\right] \frac{\theta_s^2 \overline{\ell_i}}{30}. \tag{22}$$

Average total pathlength, $\overline{\ell_1}$, over a full step, z_1, is the sum over its segments. The $\sigma_{\ell_i}^2$ are likewise summed over all segments. The Gaussian assumptions and evaluating σ_{ℓ_1} in this approximate manner appears justified since—at the point where further subdivision does not change average pathlength significantly—one expects σ_ℓ to be small. A random ℓ_{nw} is chosen from $G(\ell_{nw}|\overline{\ell_1}, \sigma_{\ell_1})$—after which the variables are adjusted once more in the manner of Eqs. 14 and 15.

Given the new pathlength, a more accurate value for the energy, ε_{nw}, at the end of the step, is obtained by rescaling linearly with pathlength

$$\varepsilon_{nw} = \varepsilon_0 + (\varepsilon - \varepsilon_0) \left(\frac{\ell_{nw}}{\overline{\ell_1}}\right). \tag{23}$$

Having determined $x, x', y, y', \varepsilon$, and ℓ_{nw}, overall transit time is found assuming the velocity, β, varies linearly over ℓ_{nw}:

$$t = \int_0^{\ell_{nw}} \frac{ds}{\beta} = \frac{\ell_{nw}}{\beta_1 - \beta_0} \log \frac{\beta_1}{\beta_0} \tag{24}$$

which, as required, approaches ℓ_{nw}/β_0 as $\beta_1 \to \beta_0$. The assumption of linear variation of β with distance traveled is strictly for convenience. It appears justified because, in the regime of interest, β is expected to vary little over one steplength.

5 Electromagnetic Fields

In general, the presence of an electromagnetic (EM) field, even in an evacuated region, is treated by numerical methods. From the Lorentz force—with

z instead of t as the independent variable:

$$\frac{d\vec{p}}{dz} = \frac{e}{\beta_z}\left(\vec{E} + \vec{\beta}\times\vec{B}\right). \tag{25}$$

Perhaps the simplest algorithm is to evaluate the fields and momenta on the right-hand sides of Eqs. 25 at the (projected) midpoint of a Monte Carlo step and take them to be constant throughout the step. After traversing a thickness z, this leads to a first order change in x':

$$x'(z) = x'_0 + \frac{e}{p_z^2}\left[(\varepsilon E_x + p_y B_z - p_z B_y) - \frac{p_x}{p_z}(\varepsilon E_z + p_x B_y - p_y B_x)\right] z \tag{26}$$

which is abbreviated as $x'(z) = x'_0 + a_x z$. To first order the displacement is

$$x(z_1) = x_0 + x'_0 z_1 + \frac{a_x}{2} z_1^2 = x_0 + \frac{x'_0 + x'(z_1)}{2} z_1 \tag{27}$$

while the energy changes by

$$\varepsilon(z_1) = \varepsilon_0 + \frac{e}{p_z}\left(\vec{p}\cdot\vec{E}\right) z_1. \tag{28}$$

This leads, via Eq. 4, to an average pathlength:

$$\begin{aligned}
\overline{\ell}_1 &= \frac{p_0}{p_z} z_1 + \left[(a_x x'_0 + a_y y'_0)\left(3 - \left(\frac{p_0}{p_z}\right)^2\right) + \left(2 - \left(\frac{p_0}{p_z}\right)^2\right)\left(\frac{p_0}{p_z}\right)\theta_s^2\right]\frac{z_1^2}{4} \\
&+ \left[2\left(a_x^2 + a_y^2\right) - 3\left(a_x x'_0 + a_y y'_0\right)^2 - \left(a_x y'_0 - a_y x'_0\right)^2\right. \\
&\quad \left. -4\left(a_x x'_0 + a_y y'_0\right)\left(\frac{p_0}{p_z}\right)\theta_s^2 - \left(\frac{p_0}{p_z}\right)^2\theta_s^4\right]\frac{z_1^3}{12} \\
&- \left(a_x^2 + a_y^2\right)\left[a_x x'_0 + a_y y'_0 + \left(\frac{p_0}{p_z}\right)\theta_s^2\right]\frac{z_1^4}{8} - \left(a_x^2 + a_y^2\right)^2\frac{z_1^5}{40}
\end{aligned} \tag{29}$$

in the presence of both matter and an EM field. It is assumed that $\sigma_{x'}^2 = \theta_s^2 p_0 z/p_z$ where all variables are evaluated at the beginning of the step. With $a_x = a_y = 0$ Eq. 29 reverts to Eq. 9. Setting $\theta_s = 0$ yields an estimate of the pathlength through an EM field *in vacuo*.

Following determination of the average pathlength the calculation proceeds similarly to the no-field case. *Random selection* of x'_1 is by the methods of [1], with $\overline{x'_1}$ given by the *in vacuo* result of Eq. 26. Given a value of x'_1, x_1 is selected from a Gaussian with mean

$$\overline{x_1} = x_0 + \frac{x'_0 + x'_1}{2} z_1 \tag{30}$$

and variance $\theta_s \overline{\ell_1}^{3/2}/2\sqrt{6}$ as for the no-field case. Given the end-values of the variables after the initial step—prior to any adjustments—an improved average pathlength is calculated using Eq 12. This is the same expression as for the no-field case since all effects of the fields are incorporated into the values of x_1 and x_1'. It is easy to confirm this explicitly by introducing the proper expectation values in the presence of EM-fields into Eq. 10 and rederive that $\overline{x'}(z)$ and $\sigma_x^2(z)$ are given by Eqs. 11 also. It then follows that Eq. 12 is the correct improved pathlength in the presence of a field as well.

As before, in subsequent stages the z-step gets repeatedly halved until stability is achieved. The procedure is the same here, except that it now requires one to re-evaluate the fields at the midpoint locations and times. After selection of a new x, x' and y, y' at the z-midpoint, via Eqs. 17 and 18, $\vec{E}$ and $\vec{B}$ are recalculated at that point. The new values for the field will change x' by

$$\Delta x' = (a_x^{nw} - a_x)\, z_1 \tag{31}$$

and x by

$$\Delta x = \frac{1}{2}\left(x_1'^{nw} - x_1'\right) z_1. \tag{32}$$

A new pathlength is determined by summing Eq. 12 over the two legs after which changes in the phase space variables are introduced as per Eqs. 14 and 15. This is repeated until the desired tolerance is met. Interfacing with more sophisticated algorithms, such as Runge-Kutta [5] or Boris [6], with the methods presented here for transport through matter appears straightforward but would require some extra work.

6 Results

A few test results obtained with the above algorithm are described in this section. One suite of such tests concerns dependence of predictions on initial step size. In the above model the basic laws assumed for large angle scattering are different from those assumed at very small angles. Their treatment also differs: collective *versus* individual simulation. These effects could influence pathlengths, etc., by amounts comparable to those arising from choice of stepsize and are therefore eliminated here and the *Gaussian approximation* for scattering is assumed to hold throughout. As a consequence, results are not expected to be accurate but now a more meaningful intercomparison becomes possible. For the energy loss algorithms this difficulty is less pronounced: the model is the same, but the treatment still

differs. To remove—as much as possible—subtle differences between collective and individual treatments (such as correlations) the (average) number of individual events per step (equivalent to stipulating a cut-off energy) is taken proportional to stepsize. The expected number of individual events for a muon traversing any part of the target is thus the same regardless of stepsize. For the collective part the (4th order) Edgeworth series is used. One could resort to a Gaussian energy loss distribution as well, per Eqs. 2 and 3, but for small enough steps this creates a problem in that it may predict some particles to *gain* energy by traversing a step in the target. For simplicity, the density effect of energy losses is neglected.

6.1 Pencil Beam on Target

A test case of a pencil beam of a 0.25 GeV/c muons incident on a 112 cm long lithium target is examined here. In Table 1 average values, standard deviations, and correlation coefficients of various characteristics of the muons at the end of the target are compared for initial step sizes of 0.2, 0.5, 1, and 2 cm. *Five* collisions per cm with electrons are treated individually. Tolerance is set at 10^{-8}, 10^{-7}, or 10^{-6} cm, i.e., estimated pathlengths corresponding to each step must agree to this value or better between successive halvings of the step length. If, at any point on the trajectory where they are calculated, a muon's polar angle or radial excursion exceeds an upper bound of 0.5 rad or 12 cm, resp., it is excluded from the simulation. A total of 10^7 incident muons are traced in each simulation with 10^{-6} or 10^{-7} cm tolerance, but only $2.5 \cdot 10^6$ for the 10^{-8} cm cases, due to CPU time considerations.

The correlations listed in Table 1 conform more or less to expectation: strong positive correlations are observed between pathlength on the one hand and radial excursion, angle, or traversal time on the other and a strong negative correlation between energy and time. The coefficient relating pathlength and energy is negative but quite weak. This confirms the expectation that energy fluctuations are dominated by variations in losses from individual $\mu - e$ encounters, while changes in pathlength play only a minor role. The overall picture presented by Table 1 is that the algorithm does it job well with respect to transverse phase space variables and pathlength: final results are essentially insensitive to choice of initial step size. However, for time and energy variables for a weak trend with initial steplength is discernible in Table 1. This is not surprising in that more care has been devoted to the transverse variables in the above algorithms. Also in this regard, the $\rho_{\ell,E}$ appear to be the least robust of the results in Table 1 with respect to stepsize or tolerance, although no clear trend emerges.

Table 1: Dependence on initial stepsize and tolerance of 0.25 GeV/c muon pencil beam characteristics after 112 cm of lithium—full algorithm

step	tol	$\langle \ell \rangle$ - Z	$\langle \theta^2 \rangle^{1/2}$	$\langle r^2 \rangle^{1/2}$	$\langle E_K \rangle$	$\langle ct \rangle$
cm	cm	cm	rad	cm	GeV	cm
0.10	10^{-6}	0.2692	0.10586	5.178	0.05276	18.532
	10^{-7}	0.2692	0.10582	5.177	0.05276	18.532
0.20	10^{-6}	0.2693	0.10590	5.178	0.05270	18.541
	10^{-7}	0.2693	0.10590	5.179	0.05270	18.541
	10^{-8}	0.2691	0.10583	5.175	0.05270	18.541
0.50	10^{-6}	0.2692	0.10588	5.177	0.05269	18.542
	10^{-7}	0.2692	0.10588	5.176	0.05269	18.541
	10^{-8}	0.2692	0.10587	5.177	0.05269	18.542
1.00	10^{-6}	0.2692	0.10589	5.178	0.05269	18.542
	10^{-7}	0.2692	0.10589	5.177	0.05269	18.542
2.00	10^{-6}	0.2692	0.10589	5.178	0.05269	18.544
	10^{-7}	0.2692	0.10590	5.177	0.05269	18.544
		σ_ℓ	σ_θ	σ_r	σ_E	σ_t
0.10	10^{-6}	0.1850	0.05515	2.581	0.00421	0.774
	10^{-7}	0.1850	0.05519	2.581	0.00421	0.774
0.20	10^{-6}	0.1851	0.05519	2.581	0.00421	0.775
	10^{-7}	0.1851	0.05519	2.581	0.00421	0.775
	10^{-8}	0.1848	0.05520	2.580	0.00421	0.775
0.50	10^{-6}	0.1850	0.05519	2.581	0.00421	0.775
	10^{-7}	0.1850	0.05519	2.580	0.00421	0.775
	10^{-8}	0.1850	0.05515	2.581	0.00421	0.775
1.00	10^{-6}	0.1850	0.05521	2.581	0.00421	0.775
	10^{-7}	0.1850	0.05520	2.581	0.00421	0.775
2.00	10^{-6}	0.1850	0.05520	2.581	0.00420	0.775
	10^{-7}	0.1850	0.05520	2.581	0.00420	0.775
		$\rho_{\ell,r}$	$\rho_{\ell,\theta}$	$\rho_{\ell,E}$	$\rho_{\ell,t}$	$\rho_{E,t}$
0.10	10^{-6}	0.9146	0.6769	-0.09771	0.3645	-0.9287
	10^{-7}	0.9146	0.6769	-0.09793	0.3648	-0.9286
0.20	10^{-6}	0.9147	0.6766	-0.09796	0.3646	-0.9288
	10^{-7}	0.9146	0.6766	-0.09829	0.3648	-0.9288
	10^{-8}	0.9145	0.6763	-0.09736	0.3636	-0.9289
0.50	10^{-6}	0.9146	0.6763	-0.09774	0.3643	-0.9289
	10^{-7}	0.9145	0.6768	-0.09822	0.3647	-0.9289
	10^{-8}	0.9146	0.6763	-0.09763	0.3641	-0.9288
1.00	10^{-6}	0.9146	0.6766	-0.09762	0.3638	-0.9291
	10^{-7}	0.9147	0.6769	-0.09761	0.3643	-0.9289
2.00	10^{-6}	0.9146	0.6770	-0.09794	0.3634	-0.9291
	10^{-7}	0.9147	0.6770	-0.09759	0.3643	-0.9290

Table 2: Dependence on stepsize of 0.25 GeV/c muon pencil beam characteristics after 112 cm of lithium—no adjustments

step	$\langle\ell\rangle$ - Z cm	σ_ℓ cm	$\langle\theta^2\rangle^{1/2}$ rad	$\langle E_{kin}\rangle$ GeV	σ_E GeV	$\rho_{\ell,E}$
0.1	0.2689	0.1848	0.10573	0.05276	0.00421	-0.09776
0.2	0.2690	0.1849	0.10578	0.05270	0.00421	-0.09827
0.5	0.2690	0.1848	0.10576	0.05269	0.00421	-0.09697
1.0	0.2690	0.1849	0.10577	0.05270	0.00421	-0.09695
2.0	0.2691	0.1849	0.10576	0.05270	0.00420	-0.09589
4.0	0.2691	0.1850	0.10572	0.05272	0.00419	-0.09440

In a *fixed step* Monte Carlo the question of optimal steplength arises: too small a step consumes needless CPU time while larger ones result in less accuracy. While a definitive answer will be highly specific to both the problem at hand and available computing resources, a general idea can be obtained by running the same test problem as above for a set of fixed step sizes. In Table 2 average and standard deviation of pathlength, rms angle, average energy and standard deviation, along with the coefficient of correlation between pathlength and energy are compared for fixed step sizes ranging from 0.1 to 4.0 cm. The algorithm takes a half-step, performs Monte Carlo selection of energy loss and scattering angle, then completes the z-step with the updated variables. Except for fixing step size, the model and its parameters are exactly as for the variable stepsize cases of Table 1. It can be seen that with dimishing step size the entries of Table 2 approach limiting values close to the variable step results of Table 1. Again $\rho_{\ell,E}$ is the least robust with respect to step size although some trend appears to be present: a 3–4% increase in $\rho_{\ell,E}$ as stepsize increases from 0.1 to 4 cm.

Of special interest to muon beam cooling are certain combinations of the characteristics listed in Tables 1 and 2, such as normalized 4-D (transverse) emittance, $\epsilon_\perp^N$, longitudinal emittance, $\epsilon_\parallel^N$, and 6-D emittance, ϵ_6^N. Table 3 compares these quantities for the same cases as Tables 1 and 2. In addition, the fraction of particles lost traversing the target—by the above criteria on angle and radial excursion—is listed for each case. Decay is *not* included as a cause of muon loss. Emittances obtained with fixed steps (marked *fixed* in tolerance column) are generally slightly lower than those resulting from variable step calculations—most notably for those with larger fixed step size. This is also true for particle losses. By this measure also, the algorithm

Table 3: $\epsilon_\perp^N$, $\epsilon_\parallel^N$, ϵ_6^N, and fraction of particles lost after 112 cm of lithium for indicated stepsize and tolerance.

step cm	tolerance	$\epsilon_\perp^N$ cm^2	$\epsilon_\parallel^N$ $GeV \cdot cm$	ϵ_6^N $GeV \cdot cm^3$	lost fraction
0.1	fixed	$5.880 \cdot 10^{-2}$	$1.1432 \cdot 10^{-2}$	$6.721 \cdot 10^{-4}$	0.019764
0.2		5.880	1.1433	6.723	0.019804
0.5		5.876	1.1422	6.711	0.019781
1.0		5.880	1.1415	6.712	0.019814
2.0		5.879	1.1390	6.696	0.019805
4.0		5.862	1.1344	6.650	0.019802
0.1	10^{-6}	5.891	1.1436	6.737	0.019831
	10^{-7}	5.889	1.1437	6.735	0.019890
0.2	10^{-6}	5.892	1.1443	6.742	0.019947
	10^{-7}	5.895	1.1439	6.744	0.019963
	10^{-8}	5.884	1.1447	6.736	0.019929
0.5	10^{-6}	5.893	1.1440	6.741	0.019966
	10^{-7}	5.888	1.1432	6.731	0.019960
	10^{-8}	5.893	1.1434	6.738	0.020068
1.0	10^{-6}	5.892	1.1423	6.730	0.020001
	10^{-7}	5.890	1.1424	6.728	0.019888
2.0	10^{-6}	5.890	1.1400	6.712	0.020004
	10^{-7}	5.889	1.1402	6.714	0.020075

appears to work better for transverse than for longitudinal emittance.

By way of illustration, further results pertaining to this example are shown in Figs. 1–7. These are derived from a Monte Carlo run with 10^6 incidents which uses the full algorithm with Edgeworth series for both energy loss (to 6th order) and angular deflection (8th order). Tolerance is set at 10^{-7} cm and initial stepsize at 0.2 cm. The density effect for energy loss is included here. The evolution of the pathlenght distribution with depth inside the target is shown in Fig. 1. It is exhibited at eight successive depths marked, in cm, on each graph. The non-Gaussian nature of the distribution is evident at any depth. The kinetic energy distribution is presented at the same eight depths in Fig. 2, which demonstrates a trend—still incomplete—towards a Gaussian distribution with increasing depth.

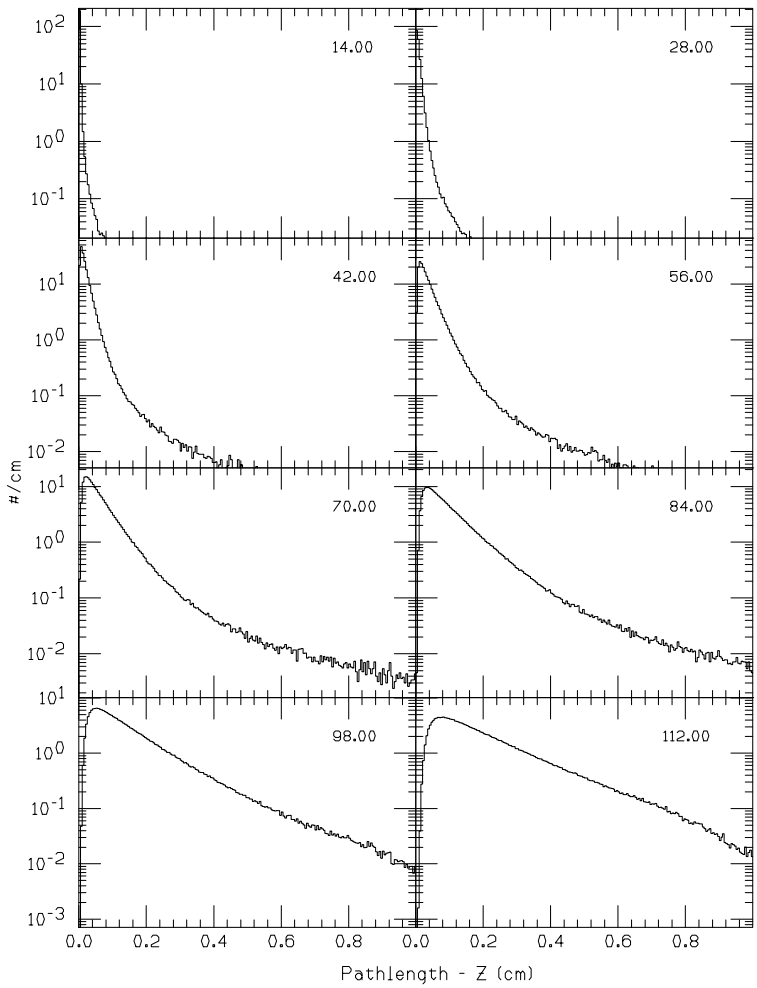

Figure 1: Evolution of pathlength distribution with distance into the target (in *cm*, indicated in each plot).

Again at the same set of depths, Fig. 3 shows the radial distribution of the muons (solid) as well as the distribution of the *maximal* radial excursion at that depth (dashes). At larger radii these graphs are hardly distinguishable. This is repeated in Fig. 4 for the angular distributions and distribution of maximal angle. As expected, these show significantly larger differences at all radii compared to the radial distributions. In practical applications, a muon traveling through a beamline, regularly interchanges angle and position, thus causing the distributions of Figs. 3 and 4 to become comingled.

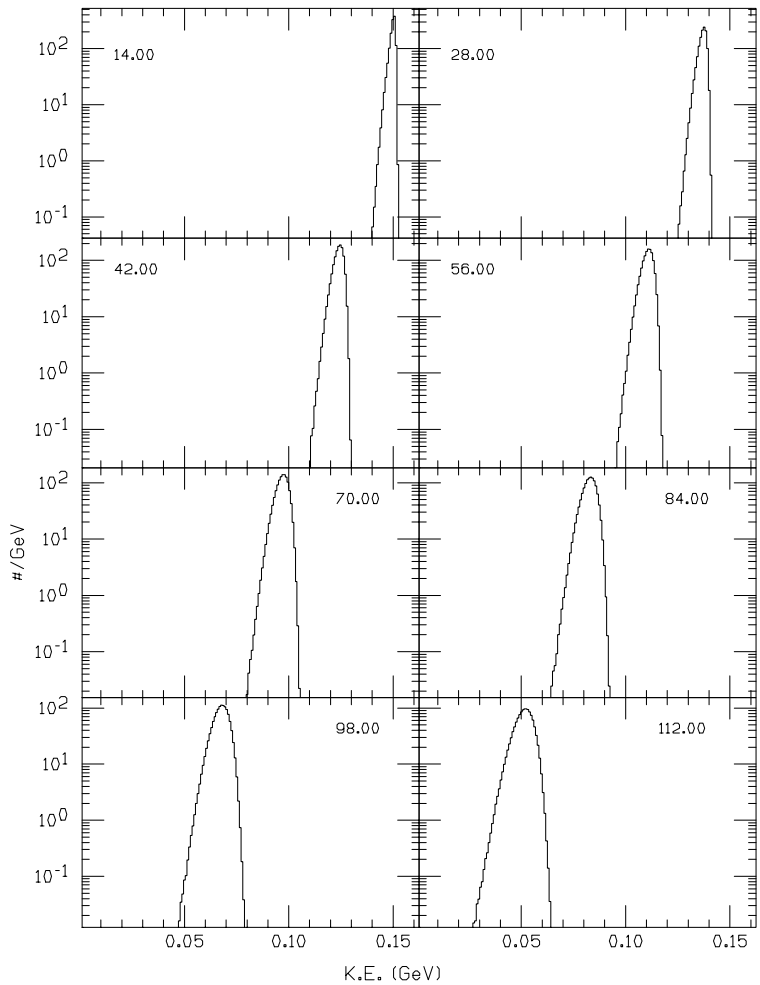

Figure 2: Evolution of kinetic energy distribution with distance into the target (in *cm*, indicated in each plot).

Scatterplots of kinetic energy *versus* pathlength are shown in Fig. 5, again at the same eight depths. A small negative correlation appears to be present in these plots.

At the exit face of the target (112 *cm*), Fig. 6 (top) shows the fraction of muons with radial coordinate above the value of the abcissa (solid) and the fraction with *maximal* radial excursion above this value (dashed) as well as the difference between the two (dotted line). This is repeated in Fig. 6 (bottom) for polar angle of the muon. These plots thus represent

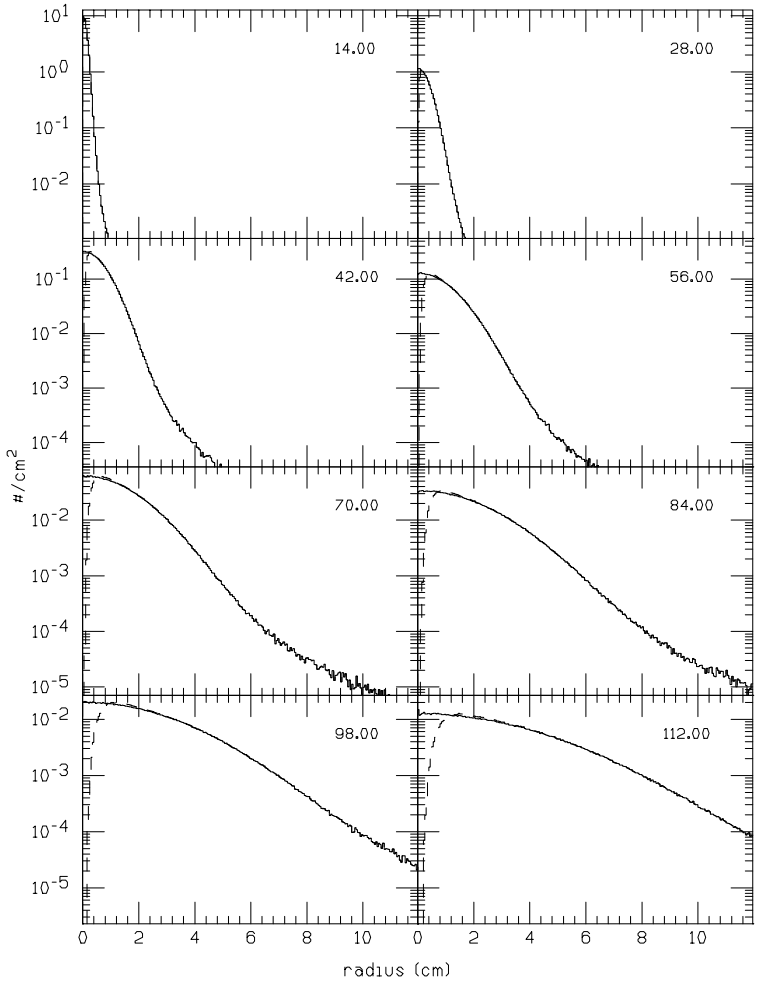

Figure 3: Evolution of radial distribution (solid) and the distribution of *maximal* radial excursion (dashed) with distance into the target (in *cm*, indicated in each plot).

the integrals for the final frames of Figs. 4 and 5 from r or θ out to their maximum values. The rather abrupt decline at the largest values of radius or angle plotted in Fig. 6 may appear somewhat puzzling. However, it should be noted that (i) there is a cut-off imposed in the calculation corresponding to the highest value of either radius or angle exhibited in each graph, (ii) radius and angle are strongly correlated: as can be seen in Table 1 both are strongly and positively correlated with pathlength so that the angular cut-off can

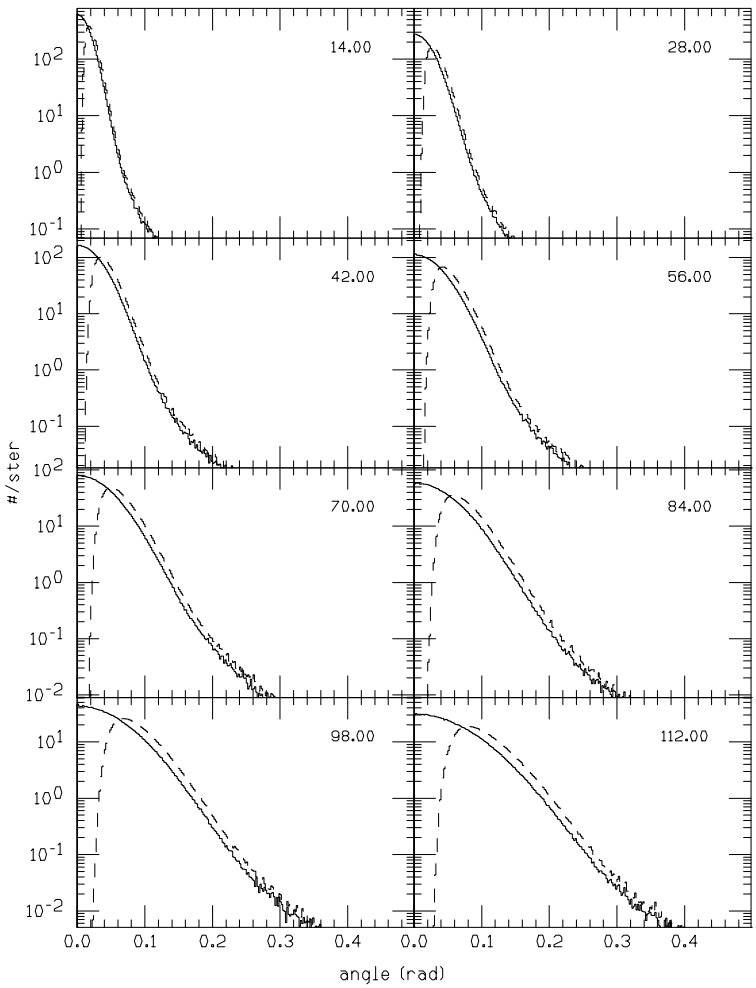

Figure 4: Evolution of angular distribution (solid) and distribution of *maximal* angular excursion (dashed) with distance into the target (in *cm*, indicated in each plot).

influence the radial one and *vice versa*, (iii) for 10^6 incidents the number of muons which explore these outer reaches is small and thus subject to considerable statistical uncertainty.

Fig. 7 presents the fraction of muons above a certain radius or angle (curve) as per legend as well as the fraction with maximal excursion above that value (plotted symbols), as function of depth (z). Again, not surprisingly, larger differences are observed for angular excursions.

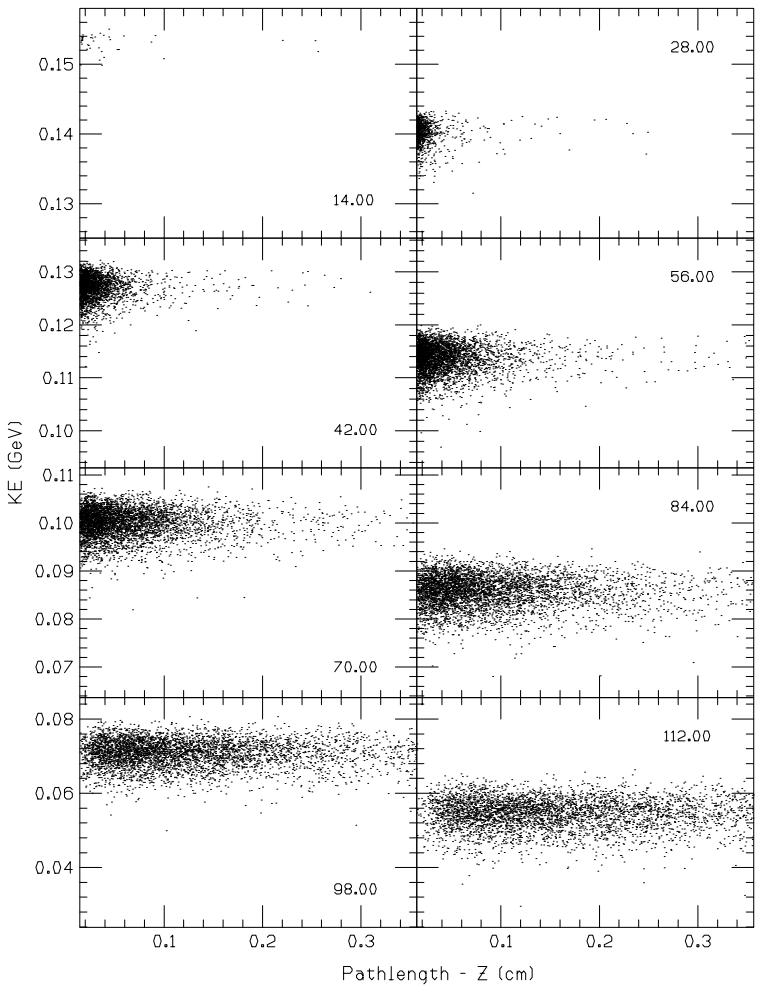

Figure 5: Evolution of kinetic energy *vs* pathlength correlation with distance into the target (in *cm*, indicated in each plot).

6.2 Repetitive Structure

The examples treated above are not representative of the repetitive structure encountered in ionization cooling. Such a repetitive structure may cause significant cancellations for certain errors of approximation while others may accumulate and become more problematic. The present purpose is only to provide an illustration and hence it is not important that beam, target, or RF be realistic representations of what might be part of an actual design.

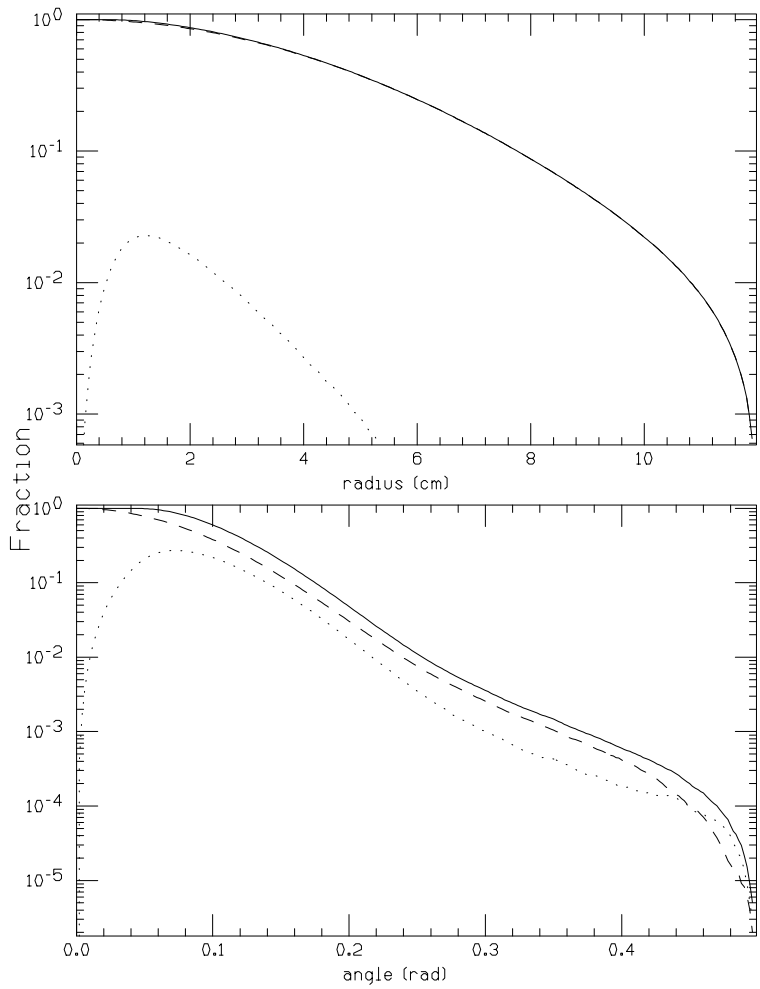

Figure 6: **top**: Fraction of muons with radial coordinate above value of abcissa at end of target (112 cm), shown as solid curve. Dashed curve indicates fraction with *maximal* radial excursion above this value. Dotted curve is difference of the two curves. **bottom**: Same as top figure but with respect to angular excursions and angle.

However, it is deemed desirable to start with a diffuse beam and to replenish the muon energy periodically so that relatively low energy muons can traverse much more material than is possible in a single pass.

The muon beam is characterized by mean longitudinal momentum $\langle p_z \rangle = 0.2\ GeV/c$ and standard deviation $\sigma_{p_z} = 0.005\ GeV/c$, with $\langle p_\perp \rangle = 0$ and

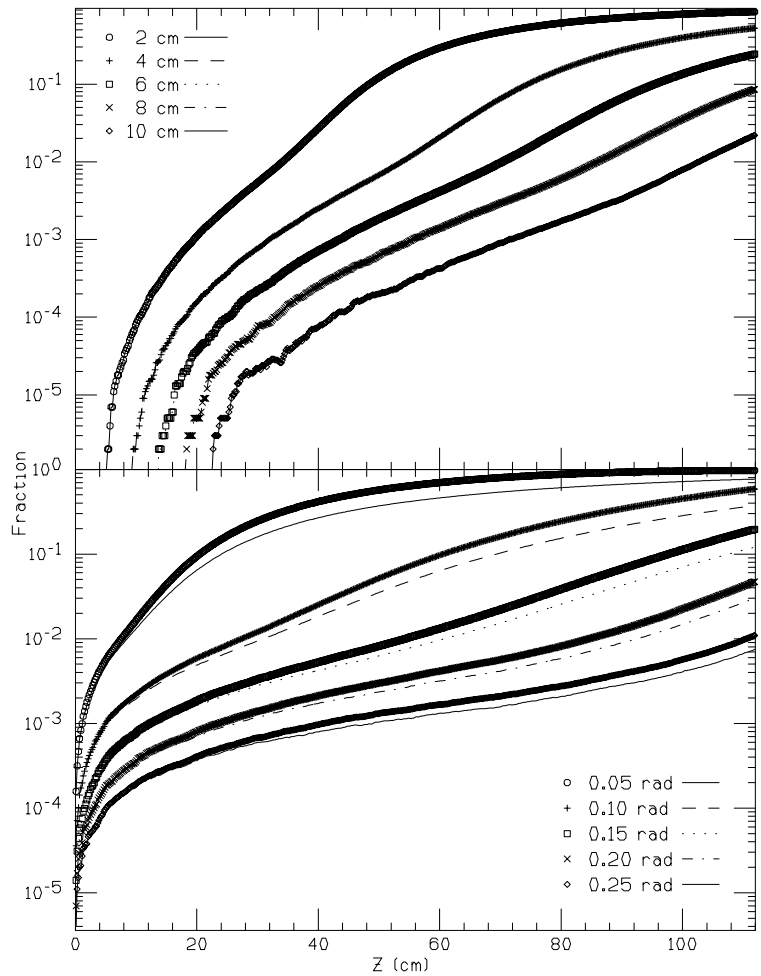

Figure 7: **top**: Fraction of muons with *prior* maximal radial excursion for each indicated value of the radius (symbols) as a function of distance into target. Also shown are the fraction of muons with radial coordinate above the indicated values (curves). **bottom**: Same as top figure but with respect to angular excursions and angle.

$\sigma_{p_\perp} = 0.005\ GeV/c$, with $\langle x \rangle = \langle y \rangle = 0$ and $\sigma_x = \sigma_y = 2\ cm$, and with $\langle t \rangle = 0$ and $\sigma_{ct} = 1\ cm$. Monte Carlo selection from the above set uses its own random number generator so that, for the same number of incidents, each case starts with the exact same beam. The above characteristics of the initial beam result in 'observed' initial emittances of $\epsilon_\perp^N = 8.955 \cdot 10^{-3}\ cm^2$,

$\epsilon_{\parallel}^{N} = 4.181 \cdot 10^{-2} cm \cdot GeV$, and $\epsilon_{6}^{N} = 3.745 \cdot 10^{-4} cm^3 \cdot GeV$. The lithium target consists of *eight* segments each 60 cm long with radius of 15 cm. In each segment an axial magnetic field of 2 $Tesla$ provides solenoidal focusing. Orbits of the muons in such a field are easily obtained analytically so that the approximate procedures of Sec. 5 are avoided along with any errors they may introduce. After each segment—including the last one—an energy boost of $0.063 + 0.005c(t - t_0)\ GeV$ is delivered to the beam exclusively along the z-direction. Here t_0 is an empirically determined average arrival time for each cavity. This energy boost is applied uniformly across the entire aperture. Muons reaching $r > 15\ cm$, $\theta > 0.5$, or p_z outside the range 0.5–1.5p_{z_0} are excluded. The beam consists of $2.5 \cdot 10^6$ muons in each simulation—except for the cases with fixed stepsize of 0.1 cm and 0.2 cm for which 10^7 are launched. Tables 4–6 present results in a manner similar to the Tables 1–3 above. Table entries correspond to values following application of the final restoring RF. This final boost clearly affects $\langle E_K \rangle$ and $\langle \theta^2 \rangle^{1/2}$ and has some influence on $\rho_{\ell,\theta}$, $\rho_{\ell,E}$ and $\rho_{E,t}$ as well.

Again the algorithms work best for transverse variables. In Table 4, the coefficients $\rho_{\ell,E}$ and $\rho_{\ell,t}$ have the opposite sign from those obtained after a single pass through a target. This can be attributed to the RF boosts which are timed to provide phase stability. Comparing the results of Tables 4 and 5 it can be seen that, for fixed steplength calculations, average pathlength and its *rms spread* are always below the ones obtained with variable stepsize. The same appears true for the *rms* angles. In this case also fixed step results show a more definite trend with stepsize. This can also be seen in Table 6 where again emittances with large (unadjusted) stepsizes are consistently low.

It should be emphazised again that the results of this section—except for those presented in the figures—use a highly simplified model which improves intercomparison but is not expected to provide accuracy.

7 Concluding Remarks

The main source of pathlength fluctuation is associated with fluctuations of scattering angle in muon-atom encounters and this appears to be adequately explored by fixed step algorithms. Two smaller sources of pathlength fluctuation are: (i) the *number* of such events fluctuates about its average, and (ii) the path of a muon as it scatters off nuclei and electrons in material is not straight line or a small set of connected straight lines and its length should be estimated more accurately than by simply adding the lengths of

Table 4: Dependence on initial stepsize and tolerance of 0.20 GeV/c diffuse muon beam characteristics after 8×60 cm of lithium—full algorithm

step cm	tol cm	$\langle \ell \rangle$ - Z cm	$\langle \theta^2 \rangle^{1/2}$ rad	$\langle r^2 \rangle^{1/2}$ cm	$\langle E_K \rangle$ GeV	$\langle ct \rangle$ cm
0.10	10^{-6}	2.1411	0.07011	6.754	0.12071	95.728
	10^{-7}	2.1400	0.07011	6.753	0.12072	95.731
0.20	10^{-6}	2.1389	0.07012	6.750	0.12068	95.733
	10^{-7}	2.1397	0.07010	6.751	0.12069	95.733
	10^{-8}	2.1391	0.07011	6.760	0.12067	95.733
0.50	10^{-6}	2.1394	0.07008	6.756	0.12068	95.735
	10^{-7}	2.1384	0.07006	6.754	0.12067	95.732
	10^{-8}	2.1380	0.07007	6.753	0.12066	95.735
1.00	10^{-6}	2.1387	0.07009	6.753	0.12067	95.731
	10^{-7}	2.1385	0.07016	6.756	0.12067	95.733
2.00	10^{-6}	2.1386	0.07010	6.754	0.12069	95.734
	10^{-7}	2.1401	0.07010	6.758	0.12070	95.735
		σ_ℓ	σ_θ	σ_r	σ_E	σ_t
0.10	10^{-6}	1.0035	0.03647	3.249	0.01161	2.178
	10^{-7}	1.0031	0.03643	3.251	0.01162	2.180
0.20	10^{-6}	1.0028	0.03649	3.251	0.01161	2.181
	10^{-7}	1.0022	0.03650	3.249	0.01161	2.181
	10^{-8}	1.0041	0.03652	3.247	0.01162	2.180
0.50	10^{-6}	1.0024	0.03646	3.251	0.01161	2.180
	10^{-7}	1.0045	0.03646	3.250	0.01162	2.180
	10^{-8}	1.0021	0.03653	3.250	0.01159	2.180
1.00	10^{-6}	1.0018	0.03649	3.251	0.01161	2.182
	10^{-7}	1.0017	0.03651	3.252	0.01161	2.181
2.00	10^{-6}	1.0020	0.03649	3.251	0.01161	2.181
	10^{-7}	1.0038	0.03651	3.255	0.01161	2.182
		$\rho_{\ell,r}$	$\rho_{\ell,\theta}$	$\rho_{\ell,E}$	$\rho_{\ell,t}$	$\rho_{E,t}$
0.10	10^{-6}	0.0424	0.3172	0.03322	-0.01066	0.5091
	10^{-7}	0.0433	0.3174	0.03336	-0.01120	0.5103
0.20	10^{-6}	0.0425	0.3179	0.03379	-0.01001	0.5102
	10^{-7}	0.0427	0.3180	0.03399	-0.01193	0.5101
	10^{-8}	0.0437	0.3180	0.03301	-0.01145	0.5107
0.50	10^{-6}	0.0427	0.3172	0.03288	-0.01190	0.5109
	10^{-7}	0.0434	0.3177	0.03417	-0.01153	0.5097
	10^{-8}	0.0423	0.3179	0.03209	-0.01089	0.5107
1.00	10^{-6}	0.0431	0.3193	0.03290	-0.01146	0.5114
	10^{-7}	0.0448	0.3190	0.03516	-0.00989	0.5101
2.00	10^{-6}	0.0429	0.3172	0.03218	-0.01234	0.5108
	10^{-7}	0.0426	0.3189	0.03344	-0.01281	0.5112

Table 5: Dependence on stepsize of 0.2 GeV/c diffuse muon beam characteristics after 8×60 cm of lithium—no adjustments

step	$\langle \ell \rangle$ - Z cm	σ_ℓ cm	$\langle \theta^2 \rangle^{1/2}$ rad	$\langle E_{kin} \rangle$ GeV	σ_E GeV	$\rho_{\ell,E}$
0.1	2.1333	0.9980	0.06997	0.12068	0.01160	0.03343
0.2	2.1343	0.9988	0.06998	0.12070	0.01159	0.03340
0.5	2.1327	0.9983	0.06995	0.12068	0.01160	0.03307
1.0	2.1335	0.9989	0.06997	0.12069	0.01160	0.03345
2.0	2.1335	0.9991	0.06997	0.12070	0.01160	0.03281
5.0	2.1346	1.0001	0.06997	0.12080	0.01161	0.03391

Table 6: $\epsilon_\perp^N$, $\epsilon_\parallel^N$, ϵ_6^N, and fraction of particles lost for diffuse muon beam after $8 \times 60cm$ of lithium for indicated stepsize and tolerance.

step cm	tolerance	$\epsilon_\perp^N$ cm^2	$\epsilon_\parallel^N$ $GeV \cdot cm$	ϵ_6^N $GeV \cdot cm^3$	lost fraction
0.1	fixed	0.27725	0.20580	0.05706	0.36578
0.2		0.27712	0.20576	0.05702	0.36535
0.5		0.27708	0.20587	0.05704	0.36569
1.0		0.27711	0.20595	0.05707	0.36517
2.0		0.27712	0.20581	0.05704	0.36399
5.0		0.27727	0.20604	0.05713	0.35883
0.1	10^{-6}	0.27806	0.20605	0.05729	0.36542
	10^{-7}	0.27791	0.20617	0.05730	0.36557
0.2	10^{-6}	0.27816	0.20614	0.05734	0.36649
	10^{-7}	0.27813	0.20621	0.05735	0.36620
	10^{-8}	0.27837	0.20615	0.05738	0.36626
0.5	10^{-6}	0.27803	0.20597	0.05727	0.36608
	10^{-7}	0.27781	0.20620	0.05728	0.36587
	10^{-8}	0.27795	0.20547	0.05711	0.36649
1.0	10^{-6}	0.27792	0.20606	0.05727	0.36617
	10^{-7}	0.27845	0.20619	0.05741	0.36578
2.0	10^{-6}	0.27815	0.20601	0.05730	0.36533
	10^{-7}	0.27863	0.20601	0.05740	0.36507

the straight segments.

Fluctuations of type (i) are mostly a concern for large angle scatterings since their numbers are small and their representation in a transport calculation may be rather crude (or absent). The influence of this on muon cooling type applications is an interesting and far-ranging question which is not pursued here. In the present Note the treatment of this effect is essentially the same for the fixed step or variable step algorithms: the number of large angle scatterings in each step is chosen from a Poisson distribution.

Type (ii) fluctuations—the main subject of this Note—do not appear to be a significant source of inaccuracy in muon cooling applications. If certain precautions are taken, fixed step size calculations yield adequate results, at least from the limited perspective of the few examples explored here.. On the other hand using a variable step size in the manner outlined above does not impose a large overhead in CPU time and has the advantage of removing the choice of steplength or at least making it less critical. A decided disadvantage is the more complicated code.

Future improvements of the present algorithm might include a better halting criterion for successive halving of the initial step. The use of a single tolerance threshold (in pathlength) may be questioned, especially if it is reached after only a small number of iterations. For example, a slight lowering of the tolerance may trigger a new round of iteration (halving of steplength) so that convergence of any given parameter as a function of tolerance may not be a smooth function of the specified tolerance. Perhaps a streamlined version of the pathlength estimation algorithm presented here may be a useful addition to the more comprehensive simulation codes.

References

[1] A. Van Ginneken, Nucl. Inst. Meth. **B160**, 460 (2000); — ,*Monte Carlo Selection of Energy Loss and Scattering Angle via Edgeworth Series*, FN-0721 (2002).

[2] B. Rossi, *High Energy Particles*, Prentice-Hall Inc., Englewood Cliffs, N.J. (1952).

[3] A. Van Ginneken, Phys. Rev. **D37**, 3292 (1988).

[4] A. Van Ginneken, Nucl. Inst. Meth. **A362**, 213 (1995).

[5] W. H. Press et al., *Numerical Recipes in* FORTRAN 2nd Ed., Cambridge Univ. Press, Cambridge, U.K. (1992).

[6] P. H. Stoltz et al., *A Boris-like Integration Scheme with Spatial Stepping*, MuCool Note 229 (2001).